The Astrophysical Journal, 772:74 (13pp), 2013 July 20 doi:10.1088/0004-637X/772/1/74

DENSITY AND ECCENTRICITY OF *KEPLER* PLANETS

Yanqin Wu[1] and Yoram Lithwick[2,3]
[1] Department of Astronomy and Astrophysics, University of Toronto, ON M5S 3H4, Canada
[2] Department of Physics & Astronomy, Northwestern University, Evanston, IL 60208, USA
[3] Center for Interdisciplinary Exploration and Research in Astrophysics (CIERA), Northwestern University, Evanston, IL 60208, USA
Received 2012 October 29; accepted 2013 May 29; published 2013 July 8

ABSTRACT

We analyze the transit timing variations (TTV) obtained by the *Kepler* mission for 22 sub-Jovian planet pairs (19 published, 3 new) that lie close to mean motion resonances. We find that the TTV phases for most of these pairs lie close to zero, consistent with an eccentricity distribution that has a very low root-mean-squared value of $e \sim 0.01$; but about a quarter of the pairs possess much higher eccentricities, up to $e \sim 0.1$–0.4. For the low-eccentricity pairs, we are able to statistically remove the effect of eccentricity to obtain planet masses from TTV data. These masses, together with those measured by radial velocity, yield a best-fit mass–radius relation $M \sim 3\,M_\oplus (R/R_\oplus)$. This corresponds to a constant surface escape velocity of $\sim$20 km s^{-1}. We separate the planets into two distinct groups: "mid-sized" (those greater than $3\,R_\oplus$) and "compact" (those smaller). All mid-sized planets are found to be less dense than water and therefore must contain extensive H/He envelopes that are comparable in mass to that of their cores. We argue that these planets have been significantly sculpted by photoevaporation. Surprisingly, mid-sized planets, a minority among *Kepler* candidates, are discovered exclusively around stars more massive than $0.8\,M_\odot$. The compact planets, on the other hand, are often denser than water. Combining our density measurements with those from radial velocity studies, we find that hotter compact planets tend to be denser, with the hottest ones reaching rock density. Moreover, hotter planets tend to be smaller in size. These results can be explained if the compact planets are made of rocky cores overlaid with a small amount of hydrogen, $\leqslant 1\%$ in mass, with water contributing little to their masses or sizes. Photoevaporation has exposed bare rocky cores in cases of the hottest planets. Our conclusion that these planets are likely not water worlds contrasts with some previous studies. While mid-sized planets most likely accreted their hydrogen envelope from the proto-planetary disks, compact planets could have obtained theirs via either accretion or outgassing. The presence of the two distinct classes suggests that $3\,R_\oplus$ could be identified as the dividing line between "hot Neptunes" and "super-Earths."

Key words: planets and satellites: composition – planets and satellites: dynamical evolution and stability – planets and satellites: formation

Online-only material: color figures

1. INTRODUCTION

The spectacular success of the *Kepler* mission (Borucki et al. 2010a, 2011; Batalha et al. 2013, hereafter B12) opens our eyes to the world of low-mass planets (also see radial velocity discoveries, e.g., Mayor et al. 2011). The *Kepler* mission has uncovered a surprising abundance of such planets close to their host stars and to each other. While some planets are inferred to have high densities and therefore are terrestrial-like, some have low densities, indicating the presence of a substantial gaseous envelope (see references in Table 3). How do these low-mass planets form and migrate? What gives rise to the range in planet radius and density? What is the internal composition of these planets? More measurements of planet density may help resolve these puzzles. In particular, ascertaining whether *Kepler* planets contain a significant amount of water would shed light on the site of their construction (see Lopez et al. 2012 for a detailed discussion).

In addition to masses, the planets' eccentricities and inclinations are valuable clues. Relative inclinations in *Kepler* systems are inferred to be only a few degrees (e.g., Tremaine & Dong 2012; Fabrycky et al. 2012; Figueira et al. 2012). This flat configuration invokes images of proto-planetary disks or planetesimal disks. Eccentricities, on the other hand, are relatively poorly constrained (see, e.g., Moorhead et al. 2011). Since eccentricities can be excited by planet interactions and damped by planet–disk interactions or tidal interactions with the host stars, they are a fossil record of past dynamical events. In Lithwick et al. (2012, hereafter Paper I), we analyze the transit time variation (TTV) signals of six planet pairs and show that the TTV phases are consistent with most planets having in general small eccentricities. More eccentricity determinations will help us rewind the clock and infer the dynamical past of these planets.

With these two goals in mind, we analyze here the TTV signals for pairs of transiting planetary candidates that lie near first-order mean-motion resonances (MMRs) using the Q0–Q6 *Kepler* table of transit times in Ford et al. (2012). We also incorporate some results from Xie (2012). We then apply our analytical TTV expressions (derived in Paper I) to infer planet properties. We introduce a new element in this work by showing how true planet density can be inferred from the nominal density measured by TTV by using statistical information from a large sample. We outline our sample selection criteria in Section 2 and discuss our results in Sections 3–5. First we recap some results from Paper I that are of relevance here.

For a pair of transiting planets that lie near a first-order MMR, mutual gravitational perturbations cause each planet's transit timing to vary sinusoidally with a sizable amplitude. The periods, amplitudes, and phases of the sinusoids encode physical properties of the planet pair.

1. The periods of the two sinusoids are the same and we call them the *super-period*:

$$P^j = \frac{1}{|j/P' - (j-1)/P|} = \frac{P'}{j|\Delta|}, \quad (1)$$

where P and P' are orbital periods of the inner and outer planets, respectively, j stands for the j:$j-1$ resonance, and $\Delta \equiv P'/P(j-1)/j - 1$ is the fractional distance to resonance. Most *Kepler* pairs with clear TTV signals have $|\Delta|$ of the order of a few percent.

2. The amplitudes ($|V|$ and $|V|'$) are functions of both planet mass and orbital eccentricity, roughly as (disregarding coefficients of the order of unity)

$$\frac{|V|}{P} \sim \frac{\mu'}{|\Delta|}\left(1 + \frac{|Z_{\rm free}|}{|\Delta|}\right),$$
$$\frac{|V'|}{P'} \sim \frac{\mu}{|\Delta|}\left(1 + \frac{|Z_{\rm free}|}{|\Delta|}\right). \quad (2)$$

Here, μ is the mass ratio between the inner planet and the star and μ' that of the outer planet. $Z_{\rm free}$ is a weighted sum of the complex free eccentricity in both planets,

$$Z_{\rm free} = f z_{\rm free} + g z'_{\rm free}, \quad (3)$$

where f and g are sums of Laplace coefficients with order-unity values, as listed in Table 3 of Paper I. The free eccentricity, $z_{\rm free}$, is the excess in eccentricity over what is forced by the resonance ("forced eccentricity"). We shall often shorten "free eccentricity" to "eccentricity," since the forced parts are mostly small for the pairs we consider ($\sim 10^{-3}$). These expressions show that amplitude ratio of the two sinusoids is roughly related to the ratio of planet masses. They also highlight an inherent problem in TTV analysis: mass and eccentricity are difficult to disentangle. However, if they could be disentangled,[4] TTV could be used to probe orbital eccentricity with a sensitivity of a couple percent ($\sim |\Delta|$). This is superior to other techniques like radial velocity or transit shape.

We define nominal masses for the two planets based on the observed TTV amplitudes,

$$m_{\rm nom} \equiv M_* \left|\frac{V'\Delta}{P'g}\right| \pi j,$$
$$m'_{\rm nom} \equiv M_* \left|\frac{V\Delta}{Pf}\right| \pi j^{2/3}(j-1)^{1/3}. \quad (4)$$

The true mass for the inner planet is $m = m_{\rm nom}/|1 - Z_{\rm free}/(2g\Delta/3)|$, and analogously for the outer planet. Hence, the nominal masses are typically upper limits: they are the true masses at zero eccentricity, but usually lie above the true masses when eccentricity is non-zero (Paper I).

3. Phases of the TTV sinusoids encode information about the free eccentricity. TTV phases are defined relative to the time when the longitude of conjunction points at the observer. The two phases ($\phi_{\rm ttv}, \phi'_{\rm ttv}$) should lie at $(0, \pi)$ for zero eccentricity,[5] while for most other eccentricities, the two phases can take other values but remain largely anti-correlated ($\phi'_{\rm ttv} \approx \phi_{\rm ttv} + \pi$). Equivalently, if the phases are close to $(0, \pi)$, then the pair likely has a small eccentricity. We show below that TTV phase can be used to infer planet eccentricity (Section 3), and consequently, genuine planet masses (Section 4).

[4] Radial velocity data, where available, can be used to break this degeneracy. Another method to do so, which we demonstrate in this paper, is to use the TTV pairs as an ensemble.

[5] From now on we call the inner planet's $\phi_{\rm ttv}$ the TTV phase.

2. A SAMPLE OF 22 PAIRS

Here we describe how our sample of 22 TTV pairs are assembled.

Transit times for quarters 0–6 are published by Ford et al. (2012) for a large number of *Kepler* candidates. We select from this list all pairs within $|\Delta| \leqslant 8\%$ from a first-order MMR (2:1, 3:2, 4:3, 5:4). For each pair, we obtain average orbital periods and TTV amplitudes and phases using the fitting procedure described in Paper I. We then calculate the periodogram for each TTV series and include a pair for further consideration only when both planets have periodograms that show a clear excess of power, by visual inspection, at the desired super-period (Equation (1)). We only include pairs with super-period shorter than 1000 days to ensure that more than half of the TTV sinusoids have been observed. Amplitudes and phases of the TTV sinusoids are measured at this super-period using a least-squares fit (Paper I). Weeding out pairs whose sinusoid phases are not roughly out of phase with each other, we find a total of 20 pairs that pass these thresholds, 6 of which are the confirmed systems analyzed in Paper I.

Compared to the exquisite TTV data for KOI 137.01/02 (Kepler-18c/d; Cochran et al. 2011), TTV data for typical *Kepler* candidates are less accurate since planets are typically smaller in size and sampled at a lower cadence. Our stringent weeding criteria are necessary to overcome random noise, and to isolate perturbations from other planets. The latter is a prominent issue in *Kepler* data, as planet pairs are often accompanied by other planets with near-resonant period ratios (e.g., KOI 82, KOI 500, and KOI 2169).

In Figure 1, we present the sinusoidal fits, error bars, and periodograms for six of the above pairs, KOI 156.01/03, KOI 775.02/01, KOI 841.01/02, KOI 1215.01/02, and KOI 1241.02/01. KOI 157.01/02, KOI 775.02/01, and KOI 1241.02/01 have also been identified as TTV pairs by Lissauer et al. (2011a) and Steffen et al. (2013) previously. For pairs that also appear in Xie (2012), we adopt his TTV fits for these systems as they are obtained using a longer baseline (through quarter 9). We also include two new pairs from that work, KOI 829.01/03 and KOI 1336.01/02, which our shorter duration data failed to pick up. However, we do not use three objects from that paper: KOI 877.01/02, KOI 880.01/02, and KOI 869.03/02; the first two because their TTV phases are not roughly anti-correlated, which may indicate pollution, and the last one because of an unphysically large density (and mass) for the inner planet: it requires a Jupiter mass for a 2.7 $R_\oplus$ planet. It is also likely contaminated by a nearby planet.

Thus, together with the 6 planet pairs analyzed in Paper I, we have a total of 22 convincing TTV pairs (19 published, 3 new). TTV solutions for these pairs, including their nominal planet masses, are listed in Table 1 and depicted in Figure 2.

2.1. Selection Effects

There are 151 planet pairs in the B12 catalog that lie within $|\Delta| \leqslant 5\%$ from a first-order MMR. Our sample of 22 pairs is $\sim$15% of the total. Since the strengths of TTV signals depend

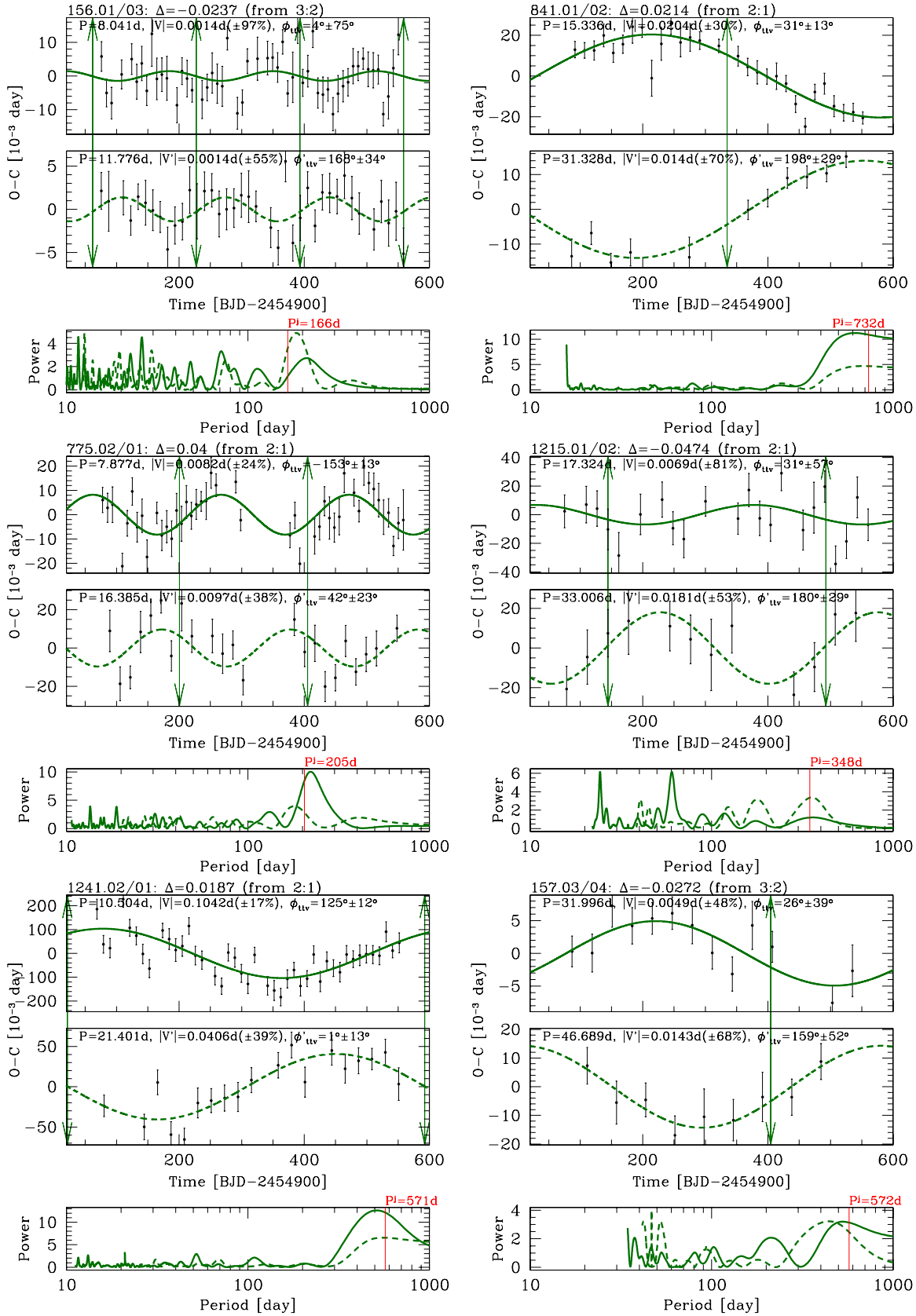

Figure 1. TTV data and periodogram for six newly identified pairs of *Kepler* candidates. For each pair, the three panels show the inner and outer planet's TTV (top and middle panels) and their periodograms (bottom). All planet candidates in this sample show clear sinusoidal variations at the desired super-period, marked by the red line in the periodogram. In the top two panels, vertical arrows are times when the longitude of conjunction points at the observer; green sinusoids are the best-fit sinusoids at the super-period; and fitted amplitudes and phases (and 68% confidence limits) are as listed, where the phase is relative to the vertical arrows. The fitting procedure is described in Paper I.

(A color version of this figure is available in the online journal.)

Table 1
TTV Analysis of 22 Planet Pairs

KOI	Δ	TTV Amplitudes (minutes)		TTV Phases (deg)		Inner Planet			Outer Planet		
		$\|V\|$	$\|V'\|$	$\phi_{\rm ttv}$	$\phi'_{\rm ttv}$	P	R	$m_{\rm nom}(M_\oplus)$	P'	R'	$m'_{\rm nom}(M_\oplus)$
137.01/02	−.028	5.27(±7%)	4.06(±10%)	−4.3(±4.0)	168.7(±5.0)	7.6420	5.49	20.20 ± 2.02	14.8590	6.98	17.17 ± 1.20
157.06/01	0.011	12.99(±40%)	4.85(±52%)	97.3(±25.2)	237.0(±34.3)	10.3040	1.89	3.87 ± 2.01	13.0250	2.92	13.69 ± 5.48
157.03/04	−.027	7.10(±48%)	20.55(±68%)	25.7(±38.8)	159.3(±52.0)	31.9960	4.37	9.68 ± 6.58	46.6890	2.60	5.14 ± 2.47
168.03/01	0.008	43.98(±37%)	18.95(±23%)	−70.1(±19.3)	123.6(±18.2)	7.1070	1.90	14.65 ± 3.37	10.7420	3.20	55.35 ± 20.48
244.02/01	0.020	3.80(±20%)	1.04(±36%)	5.7(±11.8)	200.1(±21.4)	6.2390	2.80	7.91 ± 2.85	12.7200	5.30	14.59 ± 2.92
870.01/02	0.013	11.76(±24%)	12.41(±28%)	−46.0(±14.7)	128.5(±16.6)	5.9120	2.50	12.44 ± 3.48	8.9860	2.35	19.39 ± 4.65
952.01/02	−.011	8.88(±26%)	11.15(±33%)	45.2(±15.5)	227.8(±18.3)	5.9010	2.22	7.11 ± 2.34	8.7520	2.01	8.94 ± 2.32
1102.02/01	0.009	41.03(±19%)	37.60(±25%)	−3.9(±9.5)	189.5(±14.3)	8.1460	2.74	28.39 ± 7.10	12.3330	2.90	50.58 ± 9.61
148.01/02	0.012	4.00(±27%)	3.31(±24%)	−23.5(±17.6)	199.5(±18.5)	4.7780	2.14	13.96 ± 3.35	9.6740	3.14	8.93 ± 2.41
*152.03/02	0.016	7.92(±33%)	26.21(±19%)	−29.6(±28.6)	123.2(±8.7)	13.4850	2.59	65.59 ± 12.46	27.4030	2.77	10.22 ± 3.37
248.01/02	0.010	9.22(±16%)	20.02(±8%)	54.1(±9.3)	218.0(±5.5)	7.2040	2.72	9.07 ± 0.73	10.9130	2.55	6.83 ± 1.09
500.01/02	0.012	8.50(±14%)	7.06(±22%)	−9.1(±9.0)	178.0(±13.3)	7.0530	2.64	6.31 ± 1.39	9.5220	2.79	10.88 ± 1.52
*829.01/03	0.034	16.70(±36%)	22.32(±21%)	−33.9(±11.1)	135.9(±13.0)	18.6490	2.89	92.43 ± 19.41	38.5590	3.17	30.90 ± 11.12
898.01/03	0.028	7.34(±29%)	10.80(±43%)	63.8(±15.0)	213.2(±23.3)	9.7710	2.83	44.89 ± 19.30	20.0900	2.36	14.34 ± 4.16
*1270.01/02	0.013	3.17(±36%)	37.15(±8%)	96.6(±18.5)	281.7(±4.7)	5.7290	2.19	134.49 ± 10.76	11.6090	1.55	6.03 ± 2.17
1336.01/02	0.016	18.00(±35%)	26.93(±28%)	−61.7(±17.3)	125.6(±15.8)	10.2190	2.78	24.33 ± 6.81	15.5740	2.86	26.86 ± 9.40
1589.01/02	−.016	12.82(±35%)	29.38(±26%)	21.3(±26.3)	184.6(±14.1)	8.7260	2.23	29.45 ± 7.66	12.8820	2.36	20.12 ± 7.04
156.01/03	−.024	2.07(±97%)	2.00(±55%)	3.7(±74.8)	168.4(±33.9)	8.0410	1.60	2.37 ± 1.30	11.7760	2.53	3.79 ± 3.68
*775.02/01	0.040	11.81(±24%)	13.94(±38%)	−153.1(±12.7)	40.6(±23.2)	7.8770	2.10	94.79 ± 36.02	16.3850	1.84	33.78 ± 8.11
841.01/02	0.021	29.38(±30%)	20.13(±70%)	30.5(±13.2)	198.1(±28.6)	15.3360	5.44	57.49 ± 40.24	31.3280	7.05	41.59 ± 12.48
*1215.01/02	−.047	9.86(±81%)	25.93(±54%)	29.9(±56.7)	183.8(±29.1)	17.3240	2.92	107.18 ± 57.88	33.0060	3.36	28.74 ± 23.28
*1241.02/01	0.019	149.21(±17%)	58.46(±39%)	125.9(±12.3)	360.7(±13.1)	10.5040	5.17	273.59 ± 106.70	21.4010	10.57	353.11 ± 60.03

Notes. A list of our sample of 22 TTV pairs. Here Δ is the distance to the nearest first-order MMR, $|V|$ is the measured TTV amplitude (in minutes) for the inner planet, $\phi_{\rm ttv}$ is its TTV phase (1-σ error bars in parentheses), P is its orbital period (in days), R is its radius (in $R_\oplus$), and $m_{\rm nom}$ is its nominal mass (in $M_\oplus$). The primed quantities are the same except for the outer planets. The first eight pairs are confirmed systems (corresponding to Kepler 18c/d, 11b/c, 11e/f, 23 b/c, 25 b/c, 28 b/c, 32 b/c, and 24 b/c, respectively), six of which were analyzed in Paper I. TTV parameters for the next eight pairs are adopted from Xie (2012), and TTV sinusoids for the last five pairs are reported in Figure 1. See Section 2.2 for the stellar parameters we adopt. Pairs marked with the * sign are suspected to have significant free eccentricity (Section 3). Typical error bars in planetary radii are of the order of 10%, smaller than those in TTV amplitudes. These are not included in calculating uncertainties in nominal densities.

on planet mass and eccentricity, it is of concern whether our sample is biased toward planets that have higher density or higher eccentricity when compared against planets of the same sizes and at the same periods. Moreover, we sample only planets near MMRs, which may in principle have different properties than those far from resonance.

We argue here that, in comparison with the B12 catalog, our sample favors larger planets, as well as planets that have a particular range of orbital periods, but not necessarily planets with higher density or eccentricity. First, larger planets show deeper transits and allow more precise timing. The median size of the B12 pairs is 2.18 $R_\oplus$ while our sample has a significantly larger median of 2.72 $R_\oplus$. Second, our TTV sample excludes planets with long orbital periods and hence long super-periods. It also excludes planets too close to their stars, which have smaller intrinsic TTV amplitudes and less accurate TTV measurements due to their shorter transit duration. The median inner planet period in our sample is 8.04 days, with a standard deviation of 5.98 days from the median. In contrast, values for the B12 sample are 7.88 days and 14.1 days. This means that we are mostly probing pairs clustered around ∼8 day orbital periods.

These two biases alone could explain why our sample is only 15% of the overall sample of candidate pairs. In fact, when restricting to pairs similar in properties to our sample (inner periods between 5 and 20 days, planet radii greater than 1.7 $R_\oplus$, and $|\Delta| < 5\%$), we find 48 pairs in the B12 catalog. This leaves little room to suspect that we are significantly biased toward higher density and eccentricity.

A related issue concerns sensitivity in nominal mass. Currently, *Kepler* can probe TTV signals with an amplitude upward of ∼5 minutes. Adopting $|\Delta| \approx 2\%$, and an inner period of eight days, this implies that TTVs are sensitive to planets with nominal masses upward of 5 $M_\oplus$ around a sun-like star. Sensitivity around lower mass stars is even better, ∼2 $M_\oplus$ (Figure 2), due to their deeper transit at the same planetary size. Lastly, we find that, with a factor of two longer observation, or moderate improvement in transit timing precisions, one should be able to detect TTV sinusoids in many more pairs than reported here.

We argue that our near-resonant pairs are not special. First, planet pairs in the B12 sample show similar size distribution, whether or not they are close to an MMR. Moreover, while our TTV sample is restricted to planets near first-order MMRs, the RV planets we include in our analysis below are not, and those appear to have similar properties.

2.2. Uncertainties in Stellar Parameters

Prompted by the referee, we discuss uncertainties in the stellar parameters (the most important being stellar radii) that we adopt.

There are two groups of *Kepler* host stars for which stellar radii can contain large uncertainties. The first group are stars that are hotter than 5400 K—their stellar $\log g$ values from the Kepler Input Catalog (KIC; Brown et al. 2011) are fairly uncertain as these stars can be sub-giants impersonating main-sequence stars. In this case, their radii can be underestimated

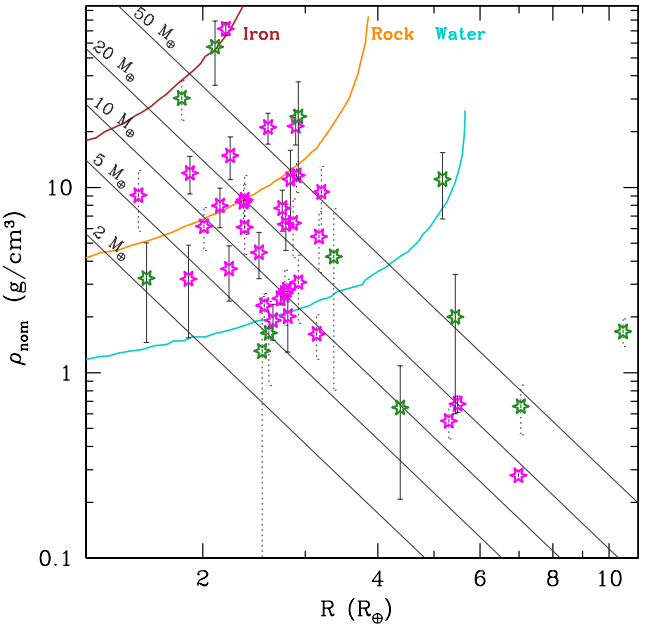

Figure 2. Nominal planet density vs. radius for the TTV sample in Table 1. Nominal densities are typically higher than true densities. The magenta stars stand for previously confirmed pairs and the green stars are those identified in this study (Figure 1). Error bars mark 68% confidence limits on the nominal densities (solid error bars for inner planets and dashed for outer). Typical uncertainties in radius are ∼10% and are not displayed here. The TTV method is currently sensitive to planet masses as small as 2 $M_\oplus$. The colored curves, marked with "Iron," "Rock," and "Water," respectively, represent the theoretical mass–radius relation for these pure compositions (Fortney et al. 2007).

(A color version of this figure is available in the online journal.)

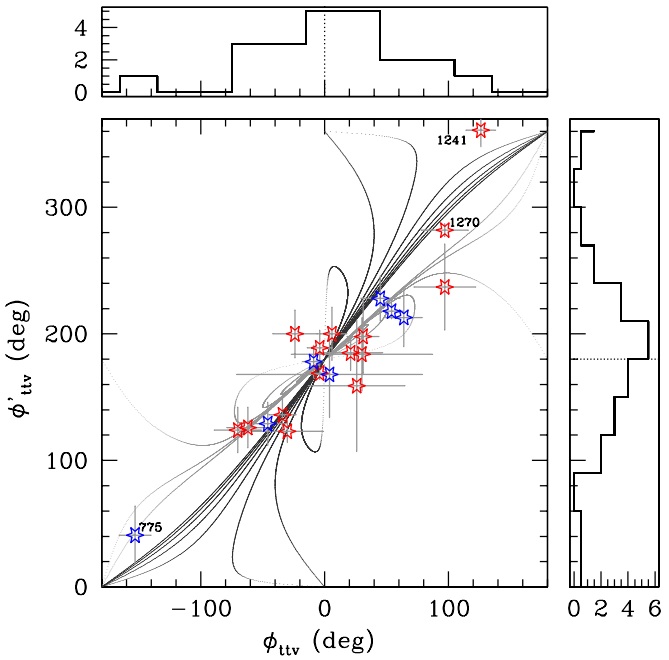

Figure 3. Phases of the TTV sinusoids for the inner ($\phi_{\rm ttv}$) and outer ($\phi'_{\rm ttv}$) planets for our 22 pairs. Pairs with very small eccentricity ($\ll |\Delta|$) would lie near (0°, 180°). For higher eccentricity, phases should lie along the various gray curves (from $0.25|\Delta|$ to $2|\Delta|$ in increments of $0.25|\Delta|$, dark gray for 2:1 MMR and lighter gray for 3:2), becoming increasingly evenly distributed along the diagonal line, which corresponds to anti-correlated phases. Histograms for the measured $\phi_{\rm ttv}$ and $\phi'_{\rm ttv}$ are displayed at the top and side panels, respectively. The measured TTV phases cluster around (0°, 180°). In this and all subsequent figures, red denotes planets around stars more massive than 0.8 $M_\odot$, and blue denotes those around less massive stars. Error bars indicate 68% confidence limit. Phases of three pairs (labeled with their KOI numbers) deviate significantly from zero. These also exhibit anomalously high nominal densities (Table 1), suggesting eccentricity $\gtrsim|\Delta|$. The pair KOI 157.06/01 (Kepler 11b/c) also has high phases (the red point at (97°, 237°)), but this likely results from its dominant resonance (5:4) being close to other nearby resonances (4:3, 6:5, etc).

(A color version of this figure is available in the online journal.)

by a factor of 1.5–2, leading to a corresponding underestimate in planet radii and an overestimate, by a factor of 3–8, in planet density.

The second group contains M dwarfs (stellar mass below 0.45 $M_\odot$) whose radii are notoriously difficult to determine due to a lack of good evolutionary tracks (see, e.g., Muirhead et al. 2012; Dressing & Charbonneau 2013). Fortunately, none of our stars are M dwarfs.

Of the 21 host stars that we study, 11 have had reliable stellar radii measurements. These include eight systems that have updated $\log g$ measurements from spectroscopy (B12): KOI 137, 148, 156, 157, 1215, 500, 841, and 898, all of which are main-sequence stars and not sub-giants (D. Huber 2012, private communication), and three systems that have asteroseismologically determined masses and radii (KOI 168, 244, and 1241; Huber et al. 2013).

For the remaining 10 stars, we adopt B12 values for the stellar radii, which are inherited from the KIC values and may contain errors. Six out of this group (KOI 248, 952, 870, 1589, 1102, and 1336) are considered to harbor low-eccentricity planets (see below) and they contribute to our final conclusion. Among these, new radii determinations (that concur with KIC values) for KOI 248 and 952 are provided by Dressing & Charbonneau (2013). KOI 870, 1102, and 1336 are confirmed systems, named as Kepler-28, Kepler-24, and Kepler-58, respectively.

Thus, while more secure stellar parameters are desirable for our systems, we believe that our basic conclusions are unlikely to be affected by their uncertainties.

3. MEASURING PLANET ECCENTRICITIES

One of the most important results from Paper I is the utility of the TTV phase ($\phi_{\rm ttv}$) for inferring the value of the free eccentricity. If a significant fraction of systems have $\phi_{\rm ttv} \approx 0$, it can be inferred that most of those have $|Z_{\rm free}| \lesssim |\Delta|$. In Paper I, we find that the TTV phases of the six analyzed pairs are clustered near zero, indicating that in general the free eccentricity is small ($|Z_{\rm free}| \leqslant \Delta$).

Now armed with 22 pairs, we explore the eccentricity distribution further. We find that for this larger sample too the TTV phases are not uniformly distributed, but cluster around zero (Figure 3), again indicating that the general population possesses small free eccentricity. However, there are a number of pairs that buck this trend. These are marked in Figure 4, based on three indices: TTV phase, nominal density, and transit duration. Both the TTV phases and nominal densities (compared to other planets of similar sizes) for KOI 775, 1241, and 1270 are large, suggesting high eccentricities. Since for the high-e population, $\phi_{\rm ttv}$ is uniformly distributed between $(-\pi, \pi)$, we expect to find pairs that have high-e but low TTV phases. Indeed, pairs KOI 152, 829, and 1215, while showing small phases, have high nominal densities. The transit durations for these planets are often longer than expected for circular orbits. We categorize these six pairs as the high-e population and analyze them in Section 5.1. It is interesting to note that all planets with nominal densities above $\sim 15\,{\rm g\,cm^{-3}}$ are now classified as high-e. The true densities of these planets are lower than the nominal values by some factors, depending on the actual eccentricities

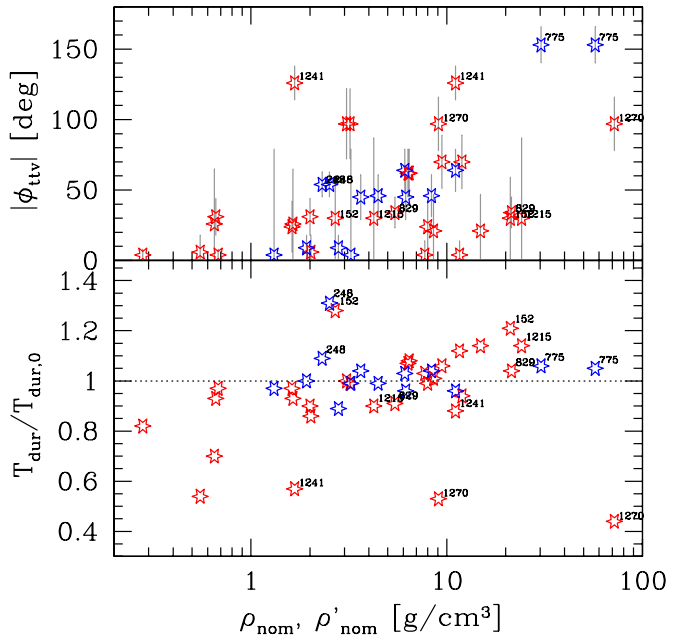

Figure 4. Identifying pairs with high eccentricity by their transit duration, nominal densities, and TTV phases. We plot TTV phase (ϕ_{ttv}, top panel) and transit duration (lower panel) vs. nominal density for all 22 pairs. The transit duration is normalized by $T_{dur,0}$, the duration of a circular orbit with zero impact parameter. All circular orbits should lie below the line of unity, while eccentric orbits can lie above or below. Three pairs (KOI 775, 1241, and 1270, marked out in Figure 3) exhibit high nominal densities, large TTV phases, and/or longer than unity transit duration. These systems almost certainly have high free eccentricities ($\gtrsim$ a few $\times\Delta$). Three pairs (KOI 152, 829, and 1215) have low TTV phases, but their high nominal densities, and in many cases, longer than unity transit duration, suggest that they possess high eccentricity. Together, these six pairs constitute our high-e population. Transits of KOI 248 last longer than expected of circular orbits. We suspect that radius determination for the host star is too small by 10%–30% (but we neglect this in the following analysis).

(A color version of this figure is available in the online journal.)

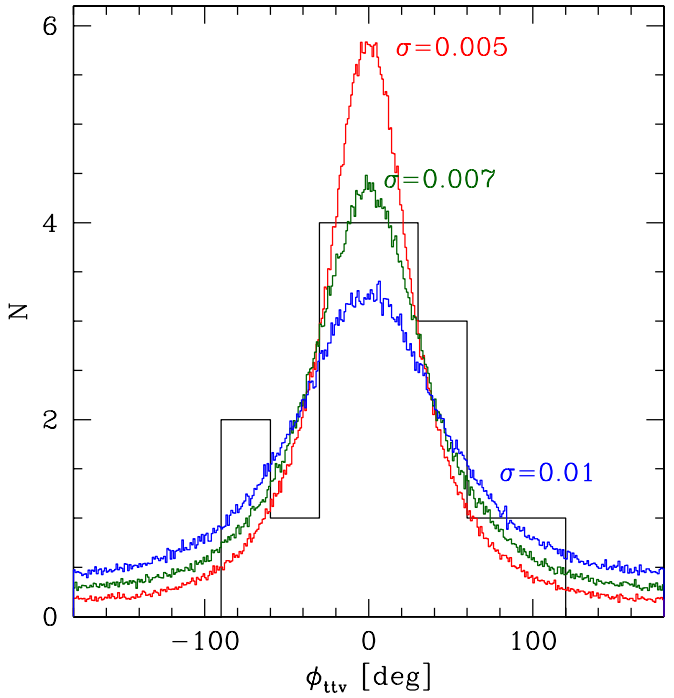

Figure 5. Distribution of TTV phases. The black histogram is the observed distribution for the 16 low-e pairs. The colored curves are simulation results at different values of eccentricity dispersion (Equation (6)), calculated for a mock catalog that has the same period ratios as the observed one. The curve with $\sigma = 0.007$ best reproduces the observation, with an uncertainty of ∼20%. The rms eccentricity of individual planets is $\sqrt{2}\sigma \approx 0.01$.

(A color version of this figure is available in the online journal.)

(Equation (2)). Unfortunately, our current strategy cannot uncover the actual eccentricities for these planets, but only lower limits.

The remaining 16 pairs (∼75%) are consistent with low eccentricity. We assume them to be a homogeneous population satisfying a single eccentricity distribution. TTV phases depend on Z_{free}, a weighted sum of the two planets' free eccentricities (Equation (3)). Splitting into real and imaginary parts,

$$z_{free} = e_x + i e_y\,, \tag{5}$$

and adopting a one-dimensional Gaussian distribution for these components (for both the inner and outer planets), $P(e_x) = P_\sigma(e_x)$, $P(e_y) = P_\sigma(e_y)$, with

$$P_\sigma(e_x) = \frac{1}{\sqrt{2\pi}\sigma}\exp\left(-\frac{e_x^2}{2\sigma^2}\right), \tag{6}$$

we can calculate the resulting distribution of TTV phases. We assume that e_x and e_y are uncorrelated, i.e., that the phases of the complex eccentricities are random, as they would be due to secular or general relativistic (GR) precession (Paper I). TTV phases are either uniformly distributed or clustered around zero, depending on the relative ratio of $\sigma/|\Delta|$, and on the resonance of relevance. Generating a mock catalog that has the same period ratios as our low-e sample, we produce different phase distributions for different values of σ (Figure 5). The current sample lead us to conclude that a value of $\sigma \approx 0.007$ provides the best fit, with an uncertainty in σ of the order of 20%. This value corresponds to an rms value of 0.01 in eccentricity ($e = \sqrt{e_x^2 + e_y^2}$). Thus, it appears that the low-e population has free eccentricities that are of order (but somewhat smaller than) the typical resonance offset ($|\Delta| \sim 0.02$).[6]

This exercise demonstrates the exceptional sensitivity of TTV measurements to even small values of eccentricity. We discuss the implication of these results in Section 5.1.

4. TRUE DENSITIES

Employing our newly found eccentricity distribution, we perform statistical simulations to correct for the eccentricity effect, and thereby obtain true planet densities for the low-e population, subject to statistical and measurement errors. Densities of the high-e sample are not recoverable.

For each planet pair, we generate complex free eccentricities (z_{free}, z'_{free}) weighted by the intrinsic distribution inferred above, with $\sigma = 0.007$ (Equation (6)). Each pair of eccentricities produces correction factors relating the true and nominal masses (see below Equation (4)). Keeping only those generated eccentricity pairs that reproduce the observed TTV phases (ϕ_{ttv}, ϕ'_{ttv}) within the 68% error bars, the median correction factor then gives the median true density. This procedure introduces an uncertainty that we quantify by the 68% bounds in the distribution of correction factors. For the total uncertainty in density measurement, we add these bounds quadratically to the error bars in TTV amplitudes. The results are listed in Table 2. The ratio

[6] We have also experimented with other forms of eccentricity distribution, e.g., a δ-function plus a Gaussian, one-dimensional Gaussian, etc., but find no improved fit to the data.

Table 2
Density after Correcting for Eccentricity Effect

KOI	ρ (g cm^{-3})	ρ' (g cm^{-3})	$\frac{\rho}{\rho_{\rm nom}}$	$\frac{\rho'}{\rho'_{\rm nom}}$	$\frac{e+e'}{2}$
137.01/02	$0.4^{+74\%}_{-52\%}$	$0.2^{+29\%}_{-28\%}$	0.66	0.82	0.007
157.06/01	$3.2^{+52\%}_{-52\%}$	$3.1^{+40\%}_{-40\%}$	1.00	1.00	0.000
168.03/01	$5.6^{+96\%}_{-65\%}$	$3.7^{+107\%}_{-73\%}$	0.47	0.40	0.008
244.02/01	$0.9^{+96\%}_{-70\%}$	$0.4^{+38\%}_{-37\%}$	0.43	0.72	0.007
870.01/02	$2.6^{+67\%}_{-54\%}$	$4.2^{+73\%}_{-55\%}$	0.57	0.50	0.008
952.01/02	$1.9^{+76\%}_{-59\%}$	$2.8^{+82\%}_{-59\%}$	0.51	0.45	0.008
1102.02/01	$3.3^{+80\%}_{-57\%}$	$4.4^{+90\%}_{-59\%}$	0.43	0.38	0.008
148.01/02	$2.2^{+95\%}_{-63\%}$	$0.9^{+53\%}_{-47\%}$	0.27	0.55	0.008
156.01/03	$2.6^{+82\%}_{-68\%}$	$1.0^{+123\%}_{-107\%}$	0.80	0.76	0.007
157.03/04	$0.5^{+87\%}_{-78\%}$	$1.3^{+82\%}_{-64\%}$	0.83	0.79	0.008
248.01/02	$1.3^{+90\%}_{-59\%}$	$1.1^{+105\%}_{-65\%}$	0.53	0.47	0.008
1336.01/02	$4.7^{+77\%}_{-58\%}$	$4.2^{+89\%}_{-65\%}$	0.74	0.65	0.008
500.01/02	$1.0^{+76\%}_{-53\%}$	$1.3^{+85\%}_{-54\%}$	0.52	0.48	0.007
841.01/02	$0.6^{+81\%}_{-79\%}$	$0.4^{+36\%}_{-37\%}$	0.32	0.63	0.009
898.01/03	$3.7^{+49\%}_{-50\%}$	$4.7^{+32\%}_{-34\%}$	0.33	0.77	0.012
1589.01/02	$9.6^{+75\%}_{-53\%}$	$5.1^{+93\%}_{-63\%}$	0.65	0.60	0.007

Notes. Planet densities after applying the statistical model for the eccentricity distribution. The column ρ lists the median density for the inner planet (and primed quantities for the outer planet), a product of the median correction factor ($\rho/\rho_{\rm nom}$) and the nominal density. Error bars on the correction factor reflect the width within which 68% of all possible solutions fall. Error bars on the median density are a quadratic sum of uncertainties in the correction factor and uncertainties in nominal mass (measurement error in TTV amplitude). The last column lists the average of the two median eccentricities as a rough indicator for the magnitude of eccentricity in the pair. Our values for KOI 137.01/02 (Kepler 18c/d) agree with previous determinations of $\rho = 0.59 \pm 0.07$, $\rho' = 0.27 \pm 0.03$ (Cochran et al. 2011). We do not perform a correction for KOI 157.06/01 (Kepler 11b/c) as its TTV phase is polluted by other resonances.

of median to nominal density depends on the observed TTV phases, but is typically of the order of 0.5. Even for planets with TTV phases consistent with zero, the correction factor falls below unity. This is because the most likely eccentricity value lies not at zero, but at $e \sim \sigma$.

The median densities and their error bars are plotted in Figure 6. Combining our results with a sample of low-mass planets that have previously determined masses (Table 3; mostly through radial velocity), we find a best-fit mass–radius relation of

$$M \approx 3\, M_\oplus \left(\frac{R}{R_\oplus}\right), \quad (7)$$

or a density $\rho \approx 3\rho_\oplus (R/R_\oplus)^{-2}$ where the density of the Earth is $\rho_\oplus = 5.5\,{\rm g\,cm^{-3}}$. This best fit differs from the one that applies for solar system planets (Lissauer et al. 2011b), $M = (R/R_\oplus)^{2.06}\, M_\oplus$, or $\rho \approx \rho_\oplus (R/R_\oplus)^{-1}$.

It is somewhat premature to discuss the significance of this difference for a number of reasons. First, we do not yet know what gives rise to the solar system scaling, or if there is anything deep behind it. Second, our mass–radius relation is only an empirical fit to a select group of planets that are situated around their host stars for 10 days, have radii $\gtrsim 1\, R_\oplus$, and masses $\sim$10–20 $M_\odot$. It may not be universally applicable. We do, however, note that the above mass–radius relation corresponds to one that has a constant surface escape velocity of 20 km s^{-1}. This is fortuitously close to the sound speed of hydrogen plasma at 10^4 K (13 km s^{-1}), suggesting that the process of photoevaporation of hydrogen may be involved in some way.

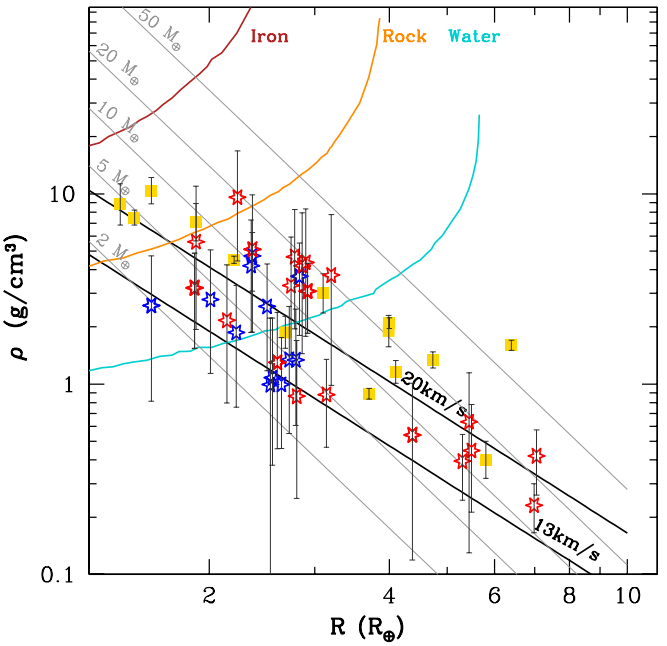

Figure 6. Similar to Figure 2, but showing the corrected densities for the 16 low-e pairs after adopting a Gaussian model for the eccentricity distribution with $\sigma = 0.007$ (Figure 5). We apply no correction for Kepler 11b/c (KOI 157.01/02). Also shown here are density measurements from Table 3 (golden squares, mostly by RV, except for Kepler 36b/c). The RV sample exhibits similar behavior to the TTV sample: larger planets are less dense, and are comparable in mass to the smaller ones. The points are best fit by the thick black line: $M = 3\, M_\oplus (R/R_\oplus)$, corresponding to a constant surface escape velocity of $v_{\rm esc} = 20\,{\rm km\,s^{-1}}$. All planets satisfy $v_{\rm esc} \gtrsim 13\,{\rm km\,s^{-1}}$, the sound speed of 10^4 K hydrogen plasma. All densities fall below $\sim$15 g cm^{-3}.
(A color version of this figure is available in the online journal.)

In the next section, we discuss further details of our findings as well as their implications.

5. DISCUSSIONS

We first divide planets into two groups: "mid-sized" (those with $R \gtrsim 3\, R_\oplus$) and "compact" (those smaller). This division line is partly inspired by an observation of the overall *Kepler* sample (B12): there is a drastic falloff in planet numbers around $3\, R_\oplus$ (right panel of Figure 8), suggesting that a transition occurs. This division is also motivated by the distinction in density between these two groups of planets: the "mid-sized" ones are lighter than water planets, while "compact" ones are of order or denser. We aim to discover the nature of this transition.

5.1. Dynamical Excitation

For the low-eccentricity population, we obtain an rms eccentricity of $e \approx 0.01$. Although small, this value is unexpected. To explain the asymmetric pile-up of planet pairs on the far side of MMRs, Lithwick & Wu (2012) and Batygin & Morbidelli (2013) argue that *Kepler* planets have experienced protracted orbital damping. This could arise, for instance, during their tenure living in disks. If this explanation is correct, the small free eccentricities observed in TTV pairs would require one to invoke a new source of eccentricity in the system to re-excite the planets.

Eccentricities for the high-e population can be estimated assuming that the true densities for these pairs follow the fiducial

mass–radius relation (Equation (7)). This yields $e \approx |z_{\rm free}| \approx (\rho_{\rm nom}/\rho_{\rm fiducial})\,|\Delta| \approx 0.1$–$0.2$.

Such high values are puzzling. To understand their origin, we look for correlations between eccentricity and other properties. We do not observe significant correlation with stellar mass, planet size, or planet period. In particular, mid-sized planets and compact planets alike contain high-e pairs. We do note that all high-e pairs reside near the 2:1 resonance. Had they been near 3:2 or even closer resonances, they might be unstable. We speculate that, while 25% of our pairs have high-e, the process that excites the eccentricities to such high values could have happened more often, but only those near 2:1 remain.

We consider the hypothesis that this high-e population arises from planet–planet scattering. If so, one expects the relative inclinations between planets to be high, since close encounters tend to excite inclinations as well as eccentricities. However, KOI 152, 775, and 829 each show three transiting planets.[7] Such a high incidence of transiting planets argues against high relative inclination in the system, and hence against planet scattering.

The presence of free eccentricity allows one to place a lower bound on the tidal quality factor in the planet[8] (Q; e.g., Goldreich & Soter 1966). Considering the high-e pair KOI 1270.01/02, for example, in order for its inner planet to retain eccentricity, it needs to have a weak tidal dissipation with $Q \geqslant 1000$, approaching the Q values estimated for gas-rich planets in our solar system ($Q \sim 10^5$). In fact, if tidal dissipation in these planets is as efficient as that in Earth (tidal quality factor $Q \approx 10$), tidal interaction between planets and the host stars should have reduced most planets' eccentricities to zero.

5.2. Mid-sized Planets, $R \geqslant 3\,R_\oplus$

5.2.1. Structure and Photoevaporation

Mid-sized planets are a minority. They comprise 23% of the total *Kepler* planet candidates.[9] Figure 6 shows that mid-sized planets are less dense than water and must have extensive H/He envelopes. Based both on the evolutionary calculations of Fortney et al. (2007) and on our simple model (see below), we conclude that the gas envelopes of these planets are comparable in mass to their solid cores (also see Gillon et al. 2007; Bakos et al. 2010; Baraffe et al. 2008 for RV planets). The actual composition of their solid cores does not affect this conclusion as the core sizes are small compared to the planet sizes.

We calculate the fractional masses in their hydrogen envelopes that are required to account for their observed densities and sizes. We assume that the cores of these planets are made of pure rock, with the core radii and masses related by Equation (7) of Fortney et al. (2007). We assume that the photospheres of all planets are at a pressure of 1 bar, and a temperature that is solely determined by irradiation, $T = T_{\rm eq}$, where $T_{\rm eq} = T_*(R_*/2a)^{1/2}$ is the equilibrium temperature of a blackbody at a distance a around a star with temperature T_* and radius R_*. We integrate the thermal structure of a solar-composition gas inward toward the core surface, using the equation of state from Saumon et al. (1995) and opacity from Allard et al. (2001). The temperature structure we obtain is nearly isothermal near the surface and adiabatic in the deep interior. The core mass is adjusted until the observed total mass is reproduced. The result depends on the assumed internal luminosity since the latter affects the temperature gradient and therefore the pressure scale height at the base of the envelope. For a luminosity of $10^{-11}L_\odot$ (the current value on Neptune), the mid-sized planets require hydrogen envelopes of order 2%–30% in mass (Figure 7). The fractions rise to 10%–90% when the internal luminosity drops by a factor of 100.

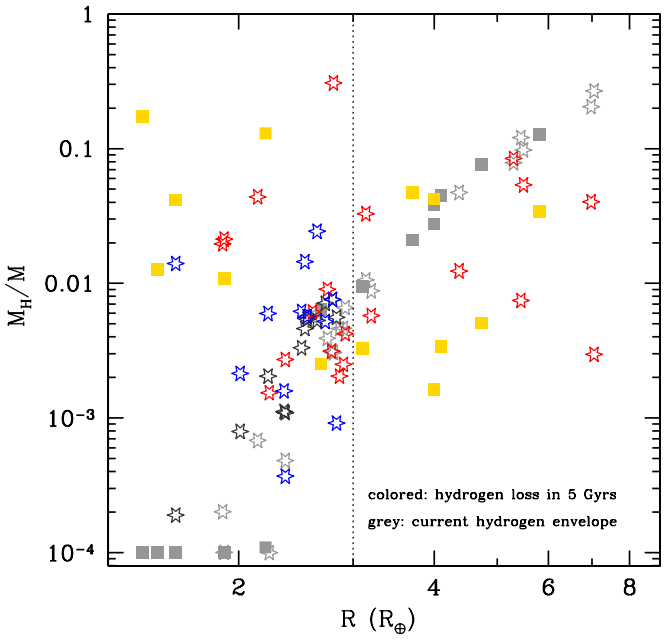

Figure 7. Hydrogen mass fractions of planets today (gray points) and those that are lost by 5 Gyr of photoevaporation (colored) for objects in Figure 6. The gray points assume that the planet is composed of a rocky core covered by a hydrogen atmosphere of solar composition, and the colored points assume that the hydrogen is eroded by energy-limited escape (Equation (8)). Given uncertainties in radius measurement, we are only sensitive to hydrogen mass fraction $\geqslant 10^{-3}$. All gray symbols falling below this value should be regarded as upper limits. For a given planet, if its gray symbol sits above its colored one, it could have retained much of its hydrogen envelope over its lifetime. While if its gray symbol sits below, as is the case for most compact objects, the planet should be a bare core.

(A color version of this figure is available in the online journal.)

The mid-sized planets exhibit surface escape velocities comparable to the sound speed of an H II region (10^4 K, 13 km s^{-1}), suggesting that photoevaporation is important for their evolution. This is corroborated by the absence of mid-sized planets with periods shorter than a few days (see Figure 11). Here, we investigate this possibility quantitatively.

We estimate mass loss due to photoevaporation following Murray-Clay et al. (2009) for X-ray and ultraviolet (XUV) photoevaporation. For more detailed treatments, see Owen & Jackson (2012); Lammer et al. (2013). Let the stellar XUV luminosity be $L_{\rm UV}$. When this flux is absorbed by the planetary atmosphere, it drives a thermal expansion and outflow. In the limit of low flux, the outflow rate can be approximated by the so-called energy-limited formula,

$$\dot{M} \approx \epsilon \frac{L_{\rm UV}\pi R_p^2}{4\pi a^2 v_{\rm esc}^2} \sim 1.2\times10^{10}\,{\rm g\ s^{-1}} \left(\frac{L_{\rm UV}}{5\times10^{-6}L_\odot}\right) \times \left(\frac{0.1{\rm AU}}{a}\right)^2 \left(\frac{R_p}{5\,R_\oplus}\right)^3 \left(\frac{15\,M_\oplus}{M_p}\right), \quad (8)$$

where we have scaled the XUV luminosity by $5\times10^{-6}L_\odot$, roughly the current solar value, and have assumed an

[7] Intriguingly, the third planets in these systems all lie close to 2:1 MMR with one of the TTV planets.

[8] We assume that dissipation in the star is irrelevant.

[9] Here, we only include candidates in systems with multiple transiting objects, as they are less polluted by false positives (Lissauer et al. 2012).

Table 3
Literature Determinations of Planet Density

Planet	R ($R_\oplus$)	M ($M_\oplus$)	ρ (g cm^{-3})	Reference
GJ1214b	2.68	6.55	1.87 ± 0.4	Charbonneau et al. (2009)
GJ3470b	4.1	14.5	1.16 ± 0.17	Bonfils et al. (2012)
GJ436b	4.0	24.3	2.09 ± 0.14	Gillon et al. (2007)
Kepler-4b	3.99	24.5	1.9 ± 0.4	Borucki et al. (2010b)
Kepler-10b	1.42	4.56	8.8 ± 2.5	Batalha et al. (2011)
HAT-P-26b	5.8	18	0.4 ± 0.1	Hartman et al. (2011)
HAT-P-11b	4.9	26	1.2 ± 0.13	Bakos et al. (2010)
CoRoT-7b	1.6	7.4	10.4 ± 1.8	Hatzes et al. (2011)
CoRoT-8b	6.4	68.7	1.6 ± 0.1	Bordé et al. (2010)
55 Cnc e	2.2	8.6	5.9 ± 1.3	Endl et al. (2012) Winn et al. (2011)
Kepler-20b	1.9	8.7	7.1 ± 1.8	Gautier et al. (2012)
Kepler-20c	3.1	16.1	3.0 ± 0.8	Gautier et al. (2012)
Kepler-36b	1.5	4.5	7.5 ± 0.7	Carter et al. (2012)
Kepler-36c	3.7	8.1	0.89 ± 0.06	Carter et al. (2012)

Notes. Transiting planets with mass determinations using the radial velocity technique (except for Kepler-36b/c, which is through TTV). Here, we only include planets that are smaller than 9 $R_\oplus$ in size.

efficiency (ϵ) of unity.[10] We have verified that the radiation/recombination-limited mass-loss rates, relevant when heat loss is significant (Murray-Clay et al. 2009), do not apply: they lie above the energy-limited rate for all our objects (compact and mid-sized). We further note that the formally defined sonic radius, $r_s = GM_p/2c_s^2$ (Parker 1965), frequently lies inside the physical radius for the low surface-escape planets we consider here.

Estimates for the fractional mass loss, integrated over 5 Gyr, are presented in Figure 7. We have uniformly taken the XUV luminosity to be 5×10^{-6} of the bolometric value, and have adopted values for stellar radius and effective temperature from the B12 catalog for the TTV planets (see Section 2.2), and from discovery papers for planets in Table 3.[11] We find that mid-sized planets could shed between a few percent to a few tenths of their masses, comparable to the hydrogen mass fractions inferred to be present on these planets (gray symbols in Figure 7). Our estimates for the mass-loss rate are for the current systems. The rates were likely higher in the past when the stars were more chromospherically active and brighter in the FUV (see, e.g., Lammer et al. 2004; Ribas et al. 2005), and also when the planets were younger and fluffier (also see Lopez et al. 2012). However, this active phase typically lasts ~100 Myr, a short interval compared to the stellar age. In addition, the fractional XUV flux may be higher for stars lower in mass than the Sun. We therefore conclude that photoevaporation has significantly sculpted these mid-sized planets. More detailed photoevaporation calculations are presented in Owen & Wu (2013).

In the following, we further argue that photoevaporation may explain the mass–radius relation for mid-sized planets (Equation (7)), and naturally produces planets with comparable core/envelope masses (also see discussions in Lopez et al. 2012).

[10] We also equate the absorption cross section to the size of the planet disk because the atmosphere pressure scale height is very small, $H/R_p \approx 0.01(R_p/2\,R_\oplus)(15\,M_\oplus/M_p)(T/1000\,\mathrm{K}) \ll 1$.

[11] Some of the stars have become sub-giants only recently, but we ignore this complication here.

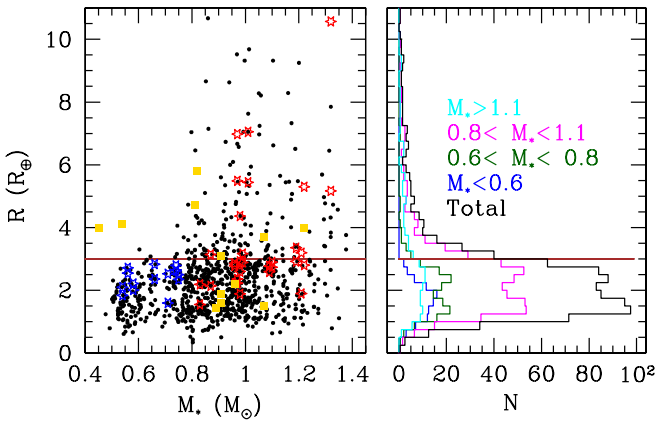

Figure 8. Size of *Kepler* planets vs. their host mass (left panel) and distribution of planet sizes (right panel). Here, we include only planet candidates from the B12 catalog that are in multiple systems (black and colored points, where the latter are the sample considered in this paper). The black histogram is the total size distribution, and the colored curves are breakdowns into different stellar mass bins. Overall, there is a precipitous drop of planet numbers at the dividing line at 3 $R_\oplus$. Mid-sized planets are absent around stars less massive than 0.8 $M_\odot$ (with the exceptions of GJ 436b and GJ 3470b, both transiting planets discovered by ground-based telescopes). As the stellar mass increases from 0.4 to 1.4 $M_\odot$, the fraction of mid-sized planets rises from 0 to unity.

(A color version of this figure is available in the online journal.)

Photoevaporation proceeds healthily, as described by Equation (8), as long as the surface escape velocity of the planet remains low. When the latter rises, the sonic radius (for a wind of ionized hydrogen) moves much beyond the planet surface. This throttles the photoevaporation rate as the radiation/recombination-limited mass-loss, now relevant, decreases exponentially with the expansion of the sonic surface (Murray-Clay et al. 2009). Now imagine a gas-rich planet that was exposed to the strong XUV flux from its young host star before it has thermally contracted, either because it was formed in situ or was migrated very quickly (Equation (8); also see Rogers et al. 2011). If such a planet started with much more gas than that in its core, evolutionary calculations (Fortney et al. 2007) show that its size will expand during mass loss, leading to further evaporation. This process continues until the mass of the solid core contributes significantly to gravity. At this point, the planet shrinks when it loses mass until the escape speed from its surface exceeds the thermal speed of ionized hydrogen. Planets thus sculpted are expected to have envelopes that are lower or comparable in mass to their cores. These arguments highlight the need for a more accurate model, where one accounts for the time evolution of both the XUV luminosity and planet structure (see, e.g., Owen & Jackson 2012).

Regardless of the evolution, the mid-sized planets almost certainly acquired their massive hydrogen envelopes by accreting from their proto-planetary disks.

5.2.2. Correlation with Stellar Mass

We focus here on one remarkable correlation between mid-sized planets and their host properties, discovered in the published *Kepler* catalog. In Figure 8, we display the distribution of planet sizes as a function of their host mass. Mid-sized planets occur almost exclusively around stars more massive than 0.8 $M_\odot$, or $T_{\rm eff} \geqslant 5000$ K on the main sequence. Quantitatively, the fraction of mid-sized planets, 23% of the overall sample, is nearly zero for stars less massive than 0.8 $M_\odot$, and of the order of half for stars more massive than 1.1 $M_\odot$. In contrast, compact planets are more equitably distributed around stars of

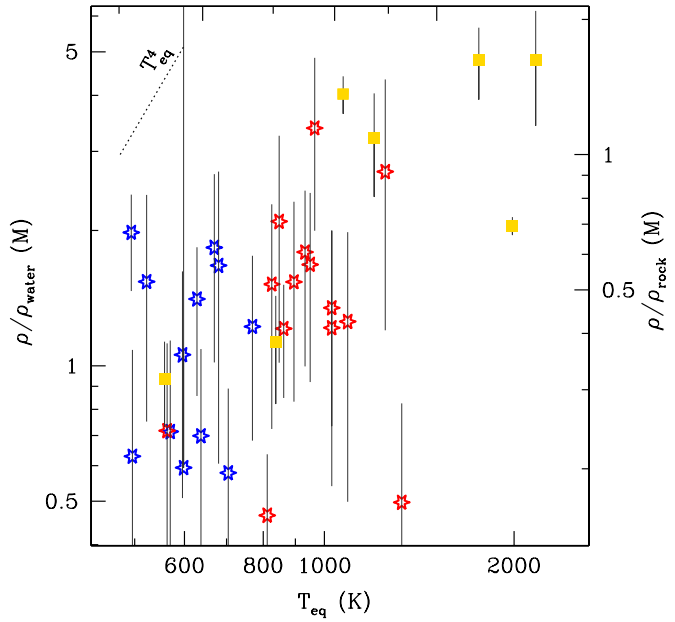

Figure 9. Hotter, compact planets are denser. We scale the density of each compact planet to that of a water sphere of the same mass (left-hand ordinate), and to a rocky sphere (right-hand ordinate). Although the densities of watery and rocky spheres are mass-dependent, the conversion factor between the two is roughly constant (Figure 6). The horizontal axis is the blackbody equilibrium temperature of the planet. We include all planets in Figure 6 that satisfy $R \leqslant 3.2\,R_\oplus$. While cool planets are roughly compatible with being water worlds, the hottest ones have densities of rock. In contrast to density, planet masses show no systematic dependence on equilibrium temperature.

(A color version of this figure is available in the online journal.)

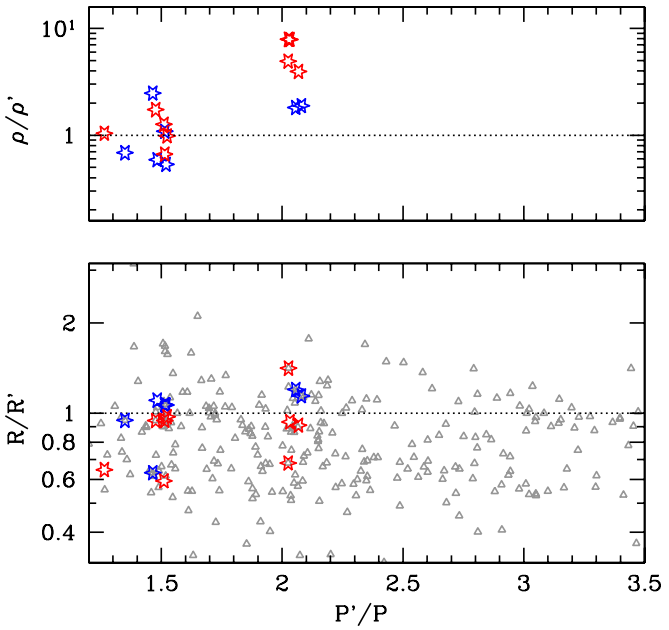

Figure 10. Properties of planet pairs plotted vs. the ratio of their orbital periods. The top panel shows the ratio of nominal density between the inner and outer planets for the compact planets in our sample. For pairs that lie close to the 2:1 MMR, the inner planets are invariably denser, while pairs around more closely spaced MMRs appear indistinguishable from each other. The bottom panel shows the size ratios for these pairs (colored points), as well as for all pairs in the B12 catalog that satisfy $P \leqslant 10$ days and where both components are compact (gray triangles). The inner planets tend to be smaller, more strikingly so when the planet pairs are spaced farther apart.

(A color version of this figure is available in the online journal.)

all spectral types, albeit with a trend that average planet sizes decrease around lower mass stars.

This result differs from that in Howard et al. (2012) where they concluded that, albeit with weak statistics, the occurrence of planets with radii larger than $4\,R_\oplus$ does not correlate with $T_{\rm eff}$. The difference may stem from the fact that while they included all candidates into their study, Figure 8 only profiles systems with multiple transiting planets. We suggest that their conclusion may be contaminated by false positives that are more populous among single transiting systems. Further studies are required to settle this difference.

The fact that K/M dwarfs do not host mid-sized, gas-rich planets[12] has not been noted previously. We offer two possible explanations but no final resolution. First, photoevaporation around lower mass stars could have been more severe than around F/G dwarfs as a result of more potent and more prolonged chromospheric activity. Second, planetary cores may take longer to form around lower mass stars, so that they cannot accrete gas before the proto-planetary disks disperse. Both scenarios can also explain why compact planets tend to be smaller around lower mass stars.

5.3. Compact Planets, $R < 3\,R_\oplus$

We turn now to the compact planets. The measured densities of compact planets range from $\sim$1 to $\sim$10 g cm^{-3} (Figure 6). The largest compact planets ($R \sim 2$–$3\,R_\oplus$) have densities that hover around the water line ($\rho \sim 2\,{\rm g\,cm^{-3}}$). At any given size, planets span almost a decade in density. While the mid-sized planets are most likely cores overlaid with massive H/He envelopes, the structure of compact planets is less certain. They can either be water–rock mixtures, or rocky cores enveloped by a small amount of hydrogen, or a mixture of the two. It is important to resolve this degeneracy because a water-laden planet would favor the scenario where the planet was constructed outside the ice line and then migrated inward; a rocky core would be consistent with in situ formation. Although density measurements of individual planets cannot break this inherent degeneracy (see, e.g., Adams et al. 2008), we attempt to break it with our statistical sample. Fortuitously, the sample straddles the region where hydrogen photoevaporation can significantly alter planet sizes.

5.3.1. Density Correlation with Temperature

Planet densities exhibit a remarkable correlation with environment: planets with hotter equilibrium temperatures are in general denser (Figure 9). In Figure 9, we scale each planet's density to the density of a pure-water (or pure-rock) planet of the same mass (see the theory curves in Figure 6).[13] Cold planets ($T_{\rm eq} \approx 600$ K) are compatible with being pure water, while hot planets ($T_{\rm eq} \geqslant 1500$ K) are compatible with being pure rock. Similar behavior has been noted by Lopez et al. (2012).

A second piece of evidence for this correlation is furnished by studying the density ratio within planet pairs (top panel of Figure 10). Unlike individual planet mass, the mass ratio of two planets within a pair can be largely determined without

[12] Gaidos et al. (2012) argued that some K/M dwarfs in the KIC are misclassified giants. If true, the sizes of their planets would increase to mid-sized. However, this would also mean that only sub-giants have mid-sized planets, which would be puzzling.

[13] If we do not scale the densities, the correlation is still present but is more scattered.

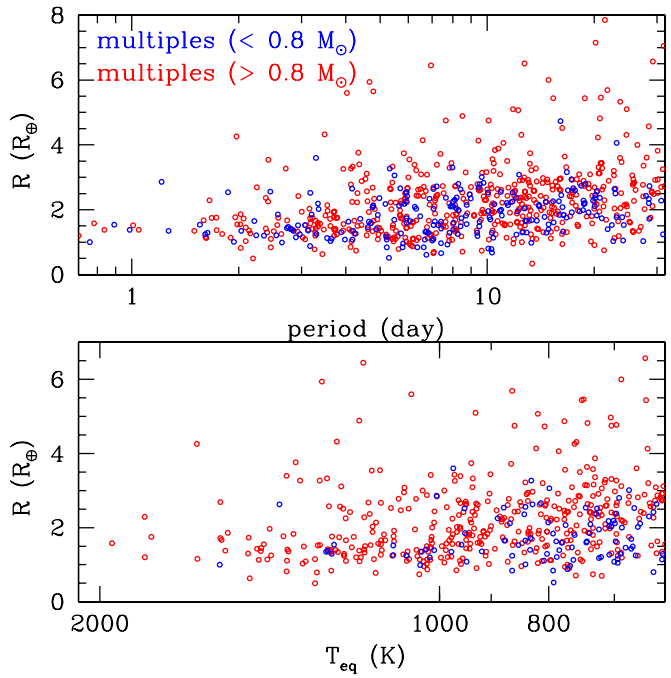

Figure 11. Planet sizes in the B12 sample plotted vs. orbital period (above) and blackbody equilibrium temperature (below). We only include systems with multiple candidates. The red points indicate those around more massive stars, and the blue points indicate those around K and M dwarfs.

(A color version of this figure is available in the online journal.)

knowledge of the free eccentricity. Thus here we simply plot the density contrast as the ratio of their nominal densities. We find that the inner planets in pairs near 2:1 resonance are always denser by a factor of a few compared to the outer ones, while pairs near closer resonances (5:4, 4:3, and 3:2) have more comparable densities.[14] Thus some process appears to be at work to systematically compactify the inner planets.

The last piece of evidence comes from studying sizes of compact planets in the B12 catalog. The bottom panel of Figure 10 shows the size ratio within a planet pair as a function of its period ratio. We only plot pairs with inner period $P < 10$ days. Inner planets tend to be smaller than their companions. This trend is more significant for more widely spaced pairs. It is absent for pairs orbiting too far from the star ($P > 10$ days). We also plot planet sizes versus orbital period or equilibrium temperature in Figure 11. One observes that compact planets farther away from their stars can be larger than those closer to their stars (also see, e.g., Figure 8 of B12). The median size for planets inward of 5 days is $R \sim 1.5\,R_\oplus$ compared with $R \sim 2.5\,R_\oplus$ for planets between 5 and 20 days. These results suggest that planets inward of ∼10 days, or ∼1000 K around a Sun-like star, show signs of compactification.

After the submission of this paper, Weiss et al. (2013) published a related study based on radial velocity data. They showed that, for planets in the mass range from a few to 20 $M_\oplus$, planet densities correlate with stellar incident flux. This is consistent with the correlation we discover here.

5.3.2. Rock or Water?

A naive explanation for Figures 9 and 10 is that all compact planets started out as water/rock mixtures with water being the dominant component, but the hottest ones have experienced total water removal and became rocky spheres.

This, however, seems difficult on theoretical grounds. It is impossible to photoevaporate water (or any other high molecular weight material). Even if heated to 10^4 K, water cannot escape from the surface of the observed planets because its sound speed would be ∼2 km s^{-1}, too low compared to the escape velocity.[15] Since the mass loss rate is determined by the smaller of the energy-limited and radiation/recombination-limited rates, and since the latter is exponentially suppressed when the sound speed is smaller than the escape speed (Murray-Clay et al. 2009), the mass loss will be severely inhibited.[16] This conclusion differs from that of Valencia et al. (2010) who adopt the energy-limited mass-loss rate for water and hence find significant water loss.

Another scenario, one that may have happened on Venus, is to photodissociate water molecules into H_2 and oxygen and then remove H_2 via either Jeans escape or hydrodynamical outflow driven by photoevaporation. This would require a reductive agent to absorb the free oxygen. If this reductive agent is atomic iron (see, e.g., Elkins-Tanton & Seager 2008), the original planet would have to contain 70% iron and 30% water in mass to absorb all free oxygen into Fe_2O_3. Such a planet, at a mass of 10 $M_\oplus$, would have a density of ∼6 g cm^{-3} (cf. the theoretical curves in Figure 2; Fortney et al. 2007), much denser than the cold planets we observe. In addition, for the newly produced hydrogen to be photoevaporated, it cannot be well mixed with the other heavy molecules. Thus we consider this option ineffective in compactifying *Kepler* planets.

Instead we propose that the observed correlations can be explained if all compact planets started out as rocky cores overlaid with various amounts of hydrogen. Planets experiencing the strongest radiation would have their hydrogen completely depleted, exposing dense rocky cores. We quantitatively investigate this possibility here.

As a useful rule of thumb, at $T_{\rm eq} = 1000$ K, a hydrogen envelope of 1% in mass will expand the size of its planet by 25%–40%, depending on the core composition and mass.[17] Another useful rule of thumb is the timescale to erode 1% of the planetary mass. We recast Equation (8) as

$$\frac{1\%M_p}{\dot{M}} \approx 5\,{\rm Gyr}\left(\frac{L_{\rm UV}}{5\times10^{-6}L_\odot}\right)^{-1} \times\left(\frac{0.1{\rm AU}}{a}\right)^{-2}\left(\frac{R_p}{2.5\,R_\oplus}\right)^{-3}\left(\frac{7.5\,M_\oplus}{M_p}\right)^{-2}, \quad (9)$$

where we have scaled the variables using typical parameters for compact planets. Since typical planets in our sample orbit with period ∼10 days, they just straddle the range where photoevaporation can make an order-unity change to their radii.

For the compact planets, mass fractions in the hydrogen envelope run from 0% to ∼1% (gray symbols in Figure 7; see assumptions for the calculations in Section 5.2.1). Figure 7 also shows that smaller compact planets in our sample could have experienced evaporation loss that ranges from 1% to 20%

[14] One notable exception is Kepler-36 where the inner planet is eight times denser than the outer one, while the two are near 6:7 resonance (Carter et al. 2012).

[15] This sound speed may increase by a factor of a few if water is photodissociated and if both hydrogen and oxygen are ionized (E. Lopez 2012, private communication). However, this does not affect our conclusion qualitatively.

[16] This argument means that the dusty evaporative clouds from KIC 12557548 (Rappaport et al. 2012) are hard to explain unless the surface escape velocity from the planet is very low (E. Chiang 2012, private communication).

[17] However, the expansion is much smaller if the hydrogen atmosphere is heavily polluted by metals. Photoevaporation is also problematic in that case.

in mass, while larger compact planets typically suffer loss of the order of 1% in mass or lower. This then makes a self-consistent story. Larger planets are larger because they can hold on to their hydrogen envelope, while smaller ones have lost it all, mostly as a result of their close proximity to the stars.

We can stretch the calculation a little further. Assuming that the planetary cores are not fully rocky (as assumed above) but are instead made up of a half-water/half-rock mixture, we would then require hydrogen mass fractions of the order of 10^{-3} or less to explain the observed planets. Such a thin atmosphere has no chance of survival for most of the planets in our sample. The situation is worse if the cores are made up of pure water. We conclude that the cores of these planets are likely composed of rock (or even denser material). This statement is substantially weakened, however, if the internal luminosity of the planet is much lower than that of Neptune.

Thus we are able to resolve the structural degeneracy in compact planets, helped by the fact that typical planets in our sample have $T_{\rm eq} \approx 1000$ K. Our proposal, that compact planets are made up of rocky cores overlaid with hydrogen $\leqslant 1\%$ in mass, explains the rock-like density of hot planets (e.g., Kepler-10b, CoRoT-7b, and 55 Cnc e), explains the factor of ~ 2 difference in size between hot and cold compact planets in the *Kepler* catalog, and explains the density contrast within 2:1 pairs and the lack of density contrast in other closer pairs.

The hydrogen mass fractions we infer for many of the compact planets are of the order of 1%. This can be primordial in origin. Alternatively, as suggested by Rogers et al. (2011) and Elkins-Tanton & Seager (2008), outgassing and the subsequent breakdown of water could produce a hydrogen envelope $\leqslant 1\%$ in mass. The former option implies a fast formation timescale, while the latter implies a significant amount of primordial water ($\geqslant 10\%$ in mass) when the planet was formed.

5.4. Rock or Water: The Lopez et al. (2012) Study

Lopez et al. (2012) study the thermal evolution of Kepler-11b, employing the energy-limited formula for photoevaporation. Their stellar FUV flux dims from 6×10^4 erg s^{-1} cm^{-2} at 100 Myr to 37 erg s^{-1} cm^{-2} at 8 Gyr. When they consider the case that Kepler-11b is a rocky sphere overlaid with hydrogen, our preferred solution here, they find that it initially had to have 30 times more hydrogen and a much bigger size (for an efficiency $\epsilon = 0.02$; see their Figure 2). They also find that if the efficiency is 0.1, the initial planet mass would have been so large as to destabilize the intricate multi-planet system (Figure 3 in that paper). They therefore conclude that Kepler-11b, with a density of 3 g cm^{-3}, is most likely a water world.

However, a concern with the Lopez et al. (2012) study is that they always adopt the energy-limited formula for mass loss. If the planet is initially $8\,R_\oplus$ and if $\epsilon = 0.02$, we find that mass loss transitions from energy-limited to radiation/recombination-limited whenever the FUV flux exceeds $\approx 10^4$ erg s^{-1} cm^{-2}. This transition occurs at an FUV flux 40 erg s^{-1} cm^{-2} if $\epsilon = 0.1$. Thus the energy-limited formula overestimates the mass loss at the critical early stage when the star was FUV bright. Taking this into account may make the initial state of Kepler-11b more probable under the no-water hypothesis than was made out in Lopez et al. (2012).

To resolve these issues, it would be desirable to conduct an evolutionary study of mass loss that includes radiation/recombination-limited mass loss rates. We leave such a study to future work.

5.5. Compact versus Mid-sized

We have suggested, based on the sharp drop-off in planet number at $R = 3\,R_\oplus$, that compact and mid-sized planets are physically distinct categories. However, the two types of planets span a similar mass range and appear to form a continuum in their density and radius (Figure 6). It is unclear what induces one, but not the other, to accrete a healthy gas envelope when both types of planets live in similar environments. We note that when a mid-sized and a compact planet coexist in a system, the former is always at least a factor of two or more massive than the latter.

6. SUMMARY

Based on two samples of low-mass planets—22 planet pairs characterized by the TTV method and a dozen planets characterized by the radial velocity technique—we reach the following conclusions.

1. TTV phases for most of our near-resonant pairs lie close to zero. We conclude that the majority of these pairs are consistent with an eccentricity distribution that has a root-mean-squared value of $e \sim 0.01$. About a quarter of the pairs, on the other hand, have eccentricities as large as 0.1–0.4. True planet masses for the low-eccentricity population can be recovered statistically, based on their inferred eccentricity distribution.
2. Masses of planets are roughly proportional to their radii, such that the best-fit solution corresponds to a population that has a constant surface escape velocity of 20 km s^{-1}.
3. Mid-sized planets ($R \geqslant 3\,R_\oplus$) in our sample invariably have such low densities that they have to contain substantial H/He envelopes. Their current rates of photoevaporation suggest that their masses and radii may have been limited by this process and that masses in their cores should be at least comparable to those of their gaseous envelopes.
4. Mid-sized planets, some 23% of the B12 sample, show up exclusively around stars more massive than $0.8\,M_\odot$. Perhaps, relatedly, planets around lower mass stars tend to have smaller sizes. We do not have an explanation for these observations.
5. Densities of compact planets ($R \leqslant 3\,R_\oplus$) fall between that of pure rock and pure water, with some even less dense than water. Planets with higher equilibrium temperatures tend to be denser and smaller. Planets in our sample fortunately straddle the region where photoevaporation could significantly erode a 1% hydrogen envelope. This allows us to break the degeneracy in internal composition and show that it is possible to explain the observed correlations if these planets are mostly likely rocky cores overlaid with a layer of hydrogen that is $\leqslant 1\%$ in mass. These planets are likely not water worlds.
6. The data suggest that $3\,R_\oplus$ is a dividing line between "super-Earths" (largely solid) and "hot Neptunes" (extensive gaseous envelopes). The atmospheres on mid-sized planets were most likely accreted, while those on compact planets may have come from accretion or outgassing.

We foresee a number of directions to pursue in the future. First, more pairs are needed. We are currently restricted to pairs in the immediate vicinity of resonances, and ones that orbit with periods of 5–12 days. Transit timing data of a longer span or a higher quality would allow one to probe many more planet pairs. It will be of interest to see whether the density–$T_{\rm eq}$

correlation (Figure 9) extends to larger ranges. More pairs will also provide a more accurate eccentricity distribution. At the moment, uncertainties in mass determination arise both from measurement errors in TTV amplitudes, and from statistical uncertainties when converting nominal mass to genuine mass.

Our conclusion that gas-rich planets appear to have suffered significant photoevaporation helps explain why there are so few of them close to the star. It also predicts that more of these gas-rich planets will show up at longer periods. The extended *Kepler* mission should be able to resolve the issue. It is also of interest to follow self-consistent thermal and photoevaporation evolution for these planets in order to determine their initial states. It remains puzzling how such low-mass planets could have accreted so much hydrogen, so close to the star. Lastly, the origin of hydrogen on compact planets is an interesting question to pursue. If it was accreted directly from the disk, these planets had to form before the disks disperse. If it was outgassed from broken-down water, these planets had to have water-rich interiors when they formed.

Most of our planets, gas-rich or compact, have masses $\lesssim 20\,M_\oplus$, a decade lower in mass than the Jovian planets at the same period range. This mass, incidentally, is roughly the gap-opening mass in a disk with a scale height $H/R \approx 0.03$. This may be a valuable clue for planet formation.

Moreover, other processes not considered in this study may be important. We argue that an icy object cannot be converted into a rocky ball. But we have not considered ice removal by bombardment of planetesimals or proto-planets.

Lastly, we need to understand the source of eccentricity in multiple low-mass planet systems.

We thank Doug Lin, Eugene Chiang, James Owen, Jonathan Fortney, Eric Lopez, and Daniel Huber for interesting discussions. Y.W. acknowledges the hospitality of KIAA-PKU, where part of this work was performed. This research is supported by NSERC and the province of Ontario, as well as NSF Grant AST-1109776. This study would not have been possible without the amazing work by the *Kepler* team.

REFERENCES

Adams, E. R., Seager, S., & Elkins-Tanton, L. 2008, ApJ, 673, 1160
Allard, F., Hauschildt, P. H., Alexander, D. R., Tamanai, A., & Schweitzer, A. 2001, ApJ, 556, 357
Bakos, G. Á., Torres, G., Pál, A., et al. 2010, ApJ, 710, 1724
Baraffe, I., Chabrier, G., & Barman, T. 2008, A&A, 482, 315
Batalha, N. M., Borucki, W. J., Bryson, S. T., et al. 2011, ApJ, 729, 27
Batalha, N. M., Rowe, J. F., Bryson, S. T., et al. 2013, ApJS, 204, 24
Batygin, K., & Morbidelli, A. 2013, AJ, 145, 1
Bonfils, X., Gillon, M., Udry, S., et al. 2012, A&A, 546, 27
Bordé, P., Bouchy, F., Deleuil, M., et al. 2010, A&A, 520, A66
Borucki, W. J., Koch, D., Basri, G., et al. 2010a, Sci, 327, 977
Borucki, W. J., Koch, D. G., Basri, G., et al. 2011, ApJ, 736, 19
Borucki, W. J., Koch, D. G., Brown, T. M., et al. 2010b, ApJL, 713, L126
Brown, T. M., Latham, D. W., Everett, M. E., & Esquerdo, G. A. 2011, AJ, 142, 112
Carter, J. A., Agol, E., Chaplin, W. J., et al. 2012, Sci, 337, 556
Charbonneau, D., Berta, Z. K., Irwin, J., et al. 2009, Natur, 462, 891
Cochran, W. D., Fabrycky, D. C., Torres, G., et al. 2011, ApJS, 197, 7
Dressing, C. D., & Charbonneau, D. 2013, ApJ, 767, 95
Elkins-Tanton, L. T., & Seager, S. 2008, ApJ, 685, 1237
Endl, M., Robertson, P., Cochran, W. D., et al. 2012, ApJ, 759, 19
Fabrycky, D. C., Lissauer, J. J., Ragozzine, D., et al. 2012, arXiv:1202.6328
Figueira, P., Marmier, M., Boué, G., et al. 2012, A&A, 541, A139
Ford, E. B., Ragozzine, D., Rowe, J. F., et al. 2012, ApJ, 756, 185
Fortney, J. J., Marley, M. S., & Barnes, J. W. 2007, ApJ, 659, 1661
Gaidos, E., Fischer, D. A., Mann, A. W., & Lépine, S. 2012, ApJ, 746, 36
Gautier, T. N., III, Charbonneau, D., Rowe, J. F., et al. 2012, ApJ, 749, 15
Gillon, M., Pont, F., Demory, B.-O., et al. 2007, A&A, 472, L13
Goldreich, P., & Soter, S. 1966, Icar, 5, 375
Hartman, J. D., Bakos, G. Á., Kipping, D. M., et al. 2011, ApJ, 728, 138
Hatzes, A. P., Fridlund, M., Nachmani, G., et al. 2011, ApJ, 743, 75
Howard, A. W., Marcy, G. W., Bryson, S. T., et al. 2012, ApJS, 201, 15
Huber, D., Chaplin, W. J., Christensen-Dalsgaard, J., et al. 2013, ApJ, 767, 127
Lammer, H., Erkaev, N. V., Odert, P., et al. 2013, MNRAS, 430, 1247
Lammer, H., Ribas, I., Grießmeier, J.-M., et al. 2004, HvaOB, 28, 139
Lissauer, J. J., Fabrycky, D. C., Ford, E. B., et al. 2011a, Natur, 470, 53
Lissauer, J. J., Marcy, G. W., Rowe, J. F., et al. 2012, ApJ, 750, 112
Lissauer, J. J., Ragozzine, D., Fabrycky, D. C., et al. 2011b, ApJS, 197, 8
Lithwick, Y., & Wu, Y. 2012, ApJL, 756, L11
Lithwick, Y., Xie, J., & Wu, Y. 2012, ApJ, 761, 122
Lopez, E. D., Fortney, J. J., & Miller, N. 2012, ApJ, 761, 59
Mayor, M., Marmier, M., Lovis, C., et al. 2011, arXiv:1109.2497
Moorhead, A. V., Ford, E. B., Morehead, R. C., et al. 2011, ApJS, 197, 1
Muirhead, P. S., Hamren, K., Schlawin, E., et al. 2012, ApJL, 750, L37
Murray-Clay, R. A., Chiang, E. I., & Murray, N. 2009, ApJ, 693, 23
Owen, J. E., & Jackson, A. P. 2012, MNRAS, 425, 2931
Owen, J. E., & Wu, Y. 2013, arXiv:1303.3899
Parker, E. N. 1965, SSRv, 4, 666
Rappaport, S., Levine, A., Chiang, E., et al. 2012, ApJ, 752, 1
Ribas, I., Guinan, E. F., Güdel, M., & Audard, M. 2005, ApJ, 622, 680
Rogers, L. A., Bodenheimer, P., Lissauer, J. J., & Seager, S. 2011, ApJ, 738, 59
Saumon, D., Chabrier, G., & van Horn, H. M. 1995, ApJS, 99, 713
Steffen, J. H., Fabrycky, D. C., Agol, E., et al. 2013, MNRAS, 428, 1077
Tremaine, S., & Dong, S. 2012, AJ, 143, 94
Valencia, D., Ikoma, M., Guillot, T., & Nettelmann, N. 2010, A&A, 516, A20
Weiss, L. M., Marcy, G. W., Rowe, J. F., et al. 2013, ApJ, 768, 14
Winn, J. N., Matthews, J. M., Dawson, R. I., et al. 2011, ApJL, 737, L18
Xie, J.-W. 2012, arXiv:1208.3312